Nickel-modified polymeric carbon nitride for improving TiO_2-based photoanode: photoelectrocatalytical evaluation and mechanistical insights

S.F. Blaskievicz [a], H.L.S. Santos [a], I.F. Teixeira [a, b], J.L. Bott-Neto [c, d], P.S. Fernández [c, d], L.H. Mascaro [a, *]

[a] Department of Chemistry, Federal University of São Carlos, 13565-905, São Carlos, SP, Brazil
[b] Max-Planck Institute of Colloids and Interfaces, Department of Colloid Chemistry, Research Campus Golm, 14424 Potsdam, Germany
[c] Chemistry Institute, State University of Campinas, PO Box 6154, 13083-970, Campinas SP, Brazil
[d] Center for Innovation on New Energies, University of Campinas, 13083-841, Campinas, SP, Brazil

ARTICLE INFO

ABSTRACT

Here, we report for the first time the synthesis of a TiO_2-based photoanode containing nickel-modified poly (heptazine imide) (Ni−PHI), a polymeric carbon nitride, as well as its application for the methanol oxidation reaction (MOR) under solar simulated and UV illumination. The photoanode was obtained initially as a thin film and the photocurrent response was evaluated in solutions containing Na_2SO_4 and methanol. For the MOR under illumination in an acidic medium, an optimal composition of the catalyst was found depositing 30-layers of TiO_2−Ni−PHI, which yielded a photocurrent of 11 mA cm^{-2} using UV radiation. The material also showed excellent stability, with a decay of approximately 5% of the photocurrent after 100 min. The improvement in the performance with Ni−PHI is likely due to the formation of a heterojunction between TiO_2 and the graphitic carbon nitride, while nickel sites act through a co-catalysis process possibly driven by *in situ* generation of nickel active species for MOR like $Ni(OH)_2|$ NiOOH. Finally, mechanistic insights into *in situ* infrared Fourier transform spectroscopy showed that TiO_2−Ni−PHI can selectively oxidize methanol to formaldehyde in the dark, while under the irradiation of UV light, the oxidized products are CO_2 and formic acid, a product with high added value.

© 2022 Elsevier Ltd. All rights reserved.

1. Introduction

Hydrogen is an environmentally friendly energy source that stands out as an attractive dense energy carrier for the future [1,2]. The methane steam reforming (the conventional method widely employed for hydrogen generation) produces large amounts of CO_2 as a by-product [3]. Photoelectrochemical (PEC) methods on the other way that can generate high purity H_2 by overall water splitting, or by organic fuel oxidation, stand out as a more sustainable and promising approach [4].

Even though the PEC methods present thermodynamic, environmental, and social advantages in comparison to pure electrochemical for the generation of H_2 [5], the performance of these devices still needs improvement to make this application feasible.

An attractive strategy is the introduction of more easily oxidized species in the medium and consequently decrease the potential for water splitting.

Small molecules such as methanol act as hole scavengers in PEC systems [6−8], leading to a photocurrent enhancement even at lower overpotentials. This process occurs because methanol (as well other small organic molecules) presents much lower oxidation potential than the oxidation of water (1.23 V vs. NHE). In this context, the methanol oxidation reaction (MOR) is a well-studied process [9−11] that presents many advantages [12], such as high efficiency and independence of a catalyst designed to cleave C−C bonds, as observed with other alcohols [13].

The use of TiO_2-based photoanodes in photo-assisted MOR emerged as a cheaper alternative to the use of noble metals, such as platinum [14,15], and it is highly encouraged, considering the high yields reported in the literature [14]. However, the high charge recombination rate hinders the technological applicability of pure TiO_2. [16,17]. This difficulty can be overcome by applying TiO_2 in

heterojunctions and composites, especially combined with a species that promotes high charge mobility such as graphene [18], carbon nanotubes [19], and polymeric carbon nitride.

Poly (heptazine imide) (PHI) is 2D sheets made of sp^2-hybridized carbon and nitrogen atoms that figure among the closest to a 'truly graphitic' carbon nitride structure [20]. The PHI is formed by heptazine units as building blocks and they can be prepared from relatively low-cost precursors (melamine and dicyandiamide) [21−23]. Due to the lone pair of electrons of the nitrogen atoms, PHI shows high electron delocalization, resulting in a unique electronic structure and a tunable band gap around 2.7 eV [24]. This band gap contributes to a promising and suitable material for the use of visible light radiation. Additionally, transition-metal ions, as nickel can be stabilized in PHI structure as coordination complexes [25,26], generating active centers formed by single atoms, which maximize the utilization of the metals (Scheme 1).

Here, we report the PEC behavior of a photoanode obtained with TiO_2 loaded with Ni−PHI. Initially, the synthesized material was obtained as a thin film and its thickness was optimized. After complete characterization and optimization, the photocurrents increased by two orders of magnitude, from 0.1 mA cm^{-2}, for the bare TiO_2 thin film, to 11 mA cm^{-2}, for the 30-layer TiO_2−Ni−PHI film. Furthermore, *in situ* infrared Fourier transform spectroscopy (FTIR) was employed to develop insights into the reaction pathway for the photoanode, where the formation of formic acid, a product of industrial interest is identified.

2. Material and methods

2.1. Synthesis of PHI and Ni−PHI

The graphitic carbon nitrides in their Na-PHI form (denoted therefore only as PHI) were prepared by the method reported by Chen et al. [22], using 1 g of melamine ground with 10 g of NaCl. In a porcelain crucible, the reaction mixture was heated, inside an oven under constant nitrogen flow (5 L min^{-1}), up to 600 °C with a heating rate of 2.3 °C min^{-1}. The temperature was held at 600 °C for 4 h, and after this time, the system was allowed to cool down. The product was removed from the crucible, washed with deionized water (1 L), isolated by filtration, and followed by complete washing with deionized water (1 L) on the filter, and then, with acetone (250 mL). After that, it was dried overnight in an oven at 60 °C.

The replacement of the sodium by nickel ions was performed by taking 0.1 g of PHI, which was suspended in 2.0 mL of water by sonication for 30 min and 1.6 mmol of $NiCl_2$ was added to the suspension. Then, the Ni−PHI samples were extensively washed with deionized water (approximately 250 mL) and acetone (50 mL). The photocatalysts were separated by centrifugation in a 2 mL plastic tube (11,000 rpm, for 5 min) and dried overnight in an oven at 60 °C [25].

2.2. Preparation of photoanodes

The photoanodes were produced in the form of thin films. First, 2.5% (wt. %) of carbon nitride (PHI and Ni−PHI) was added to a commercial titania paste (Sigma-Aldrich), in summary, 0.5 g of the commercial paste mixed with 0.0125 g of the selected carbon nitride and 3.5 g of ethanol. Then, the prepared paste was spin-coated onto an fluorine-doped tin oxide (FTO) electrode, dropping 100 μL of the material onto the FTO and stirring at 3000 rpm for 30 s. After that, the films underwent thermal annealing to improve the adhesion of the film on the FTO and remove the organic thickeners from the paste (ethylcellulose and α-terpineol) for 20 min at 400 °C in air, at a heating rate of 5 °C min^{-1}, starting from room temperature. The samples were named TiO_2−PHI (TiO_2 containing PHI) and TiO_2−Ni−PHI (TiO_2 containing Ni−PHI). For comparison, films formed by only PHI and Ni−PHI were produced under the same conditions, using PEG300 (Sigma-Aldrich) as a dispersing agent. For further studies, the process of TiO_2−Ni−PHI deposition was repeated to obtain samples with 8, 15, and 30 layers deposited.

A glassy carbon electrode was used in the *in situ* FTIR measurements, which was polished carefully to a mirror finish and cleaned ultrasonically in deionized water for 5 min. The TiO_2−Ni−PHI film was obtained following the same deposition procedure with the paste being spin-coated over the electrode surface and thermally annealed for 20 min at 400 °C in air.

2.3. Characterization of the samples

The carbon monoxide diffuse reflectance infrared Fourier transform spectroscopy (CO DRIFTS) FTIR experiments were carried out with a Spectra Tech high-temperature cell containing a CaF_2 window, which was coupled to a Thermo Nicolet spectrophotometer IS50 FTIR with a Mercury−Cadmium Tellurium detector. Each
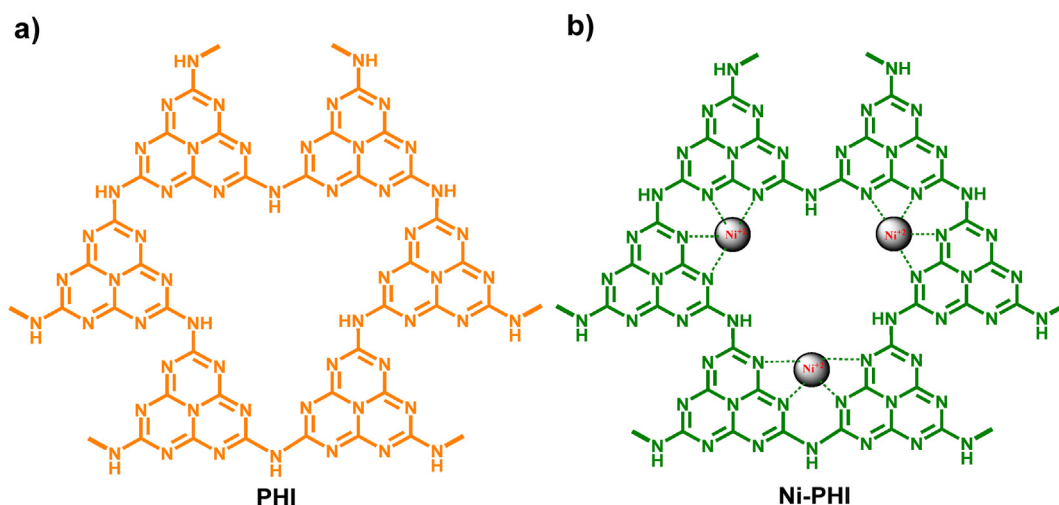
Scheme 1. Illustration of the structure of (**a**) PHI and (**b**) PHI containing atomically dispersed nickel II sites (Ni−PHI). PHI, poly (heptazine imide).

sample was placed in the cell and heated up to 350 °C under He flow, being purged with pure He gas at 350 °C for 10 min, and then cooled down to room temperature, still under He flow (20 mL min^{-1}). First, the room temperature background spectrum was recorded under He flow, followed by the introduction of pure CO into the cell for 0.5 h at a flow rate of 10 mL min^{-1} for the spectrum measurement under constant CO flow. The CHN elemental analysis was carried out by combustion analysis using a Vario Micro device. The concentration of nickel was determined using atomic absorption spectrophotometry (Hitachi-Z8200 spectrophotometer). FTIR with attenuated total reflection (ATR) spectra were recorded on a Varian1000 FTIR spectrophotometer equipped with an ATR unit made of diamond, applying a resolution of 4 cm^{-1}. Diffuse reflectance UV−vis spectroscopy data were obtained with a Cary 5E spectrophotometer, with the wavelength operating from 300 to 800 nm. The X-ray diffraction (XRD) measurements were made in a Shimadzu diffractometer model XRD-6000 in θ-2θ mode, from 10 to 80° with a rate of 1 deg min^{-1} and an electrode voltage of 30 kV. The morphology and thickness of the obtained films were analyzed in a high-resolution field emission scanning electron microscope (Zeiss Supra at 2 kV). Transmission electron microscopy (TEM) analyses were conducted in a JEOL JEM 2100F. The photoanode film was immersed in a beaker containing isopropyl alcohol and submitted to an ultrasonic bath for 10 min. The resulting suspension was dropped in a holy-carbon grid for the TEM analysis. For the X-ray photoelectron spectroscopy (XPS) measurements, a Scienta Omicron spectrometer, model ESCA 2SR, was employed with an Mg K-α monochromator to provide the incident photon energy, calibrated using the C 1s peak (284.8 eV). Raman spectra were performed with a micro-Raman Horiba Jobin Yvon (HR 550) system with a 514.5 nm wavelength incident argon laser light, coupled with an optical microscope (Olympus BX41). Mott-Schottky analysis was performed by measuring impedance spectra of the samples in a potential range from 0.75 to −1.50 V RHE, −0.02 V potential step, 7 mV potential amplitude, and frequencies from 10 kHz to 0.1 Hz. The measurements were performed in a standard three-compartment electrochemical cell using a Pt plate and silver/silver chloride (Ag/AgCl) in saturated KCl as the counter and reference electrodes, respectively, using 0.5 mol L^{-1} H$_2$SO$_4$ as the electrolyte. The system was previously purged and maintained with constant nitrogen gas flow during the measurement. The same electrochemical system was also employed for illuminated open circuit potential measurements, where chronopotentiometry was recorded using a solar simulator (LCS-100 − Newport), with irradiances of 0, 100, 200, 400, and 500 mW cm^{-2}.

2.4. PEC studies

The performance of the photoanodes was evaluated for both the OER and MOR. A three-electrode cell was used for the PEC measurements. A Pt plate was used as the counter electrode and silver/silver chloride (Ag/AgCl) in saturated KCl (E°$_{Ag/AgCl}$ = +0.197 V vs. NHE − normal hydrogen electrode) was employed as the reference electrode. Linear sweep voltammograms were measured at 10 mV s^{-1}, with light chopped at the front side of the electrode using a solar simulator (LCS-100 - Newport, with an irradiance of 100 mW cm^{-2}) and a light-emitting diode (LED) UV LED M365LP1 − Thorlabs, with λ = 365 nm and an irradiance of 90 mW cm^{-2}) as light sources. For the OER reaction, Na$_2$SO$_4$ 0.5 mol L^{-1} (pH 6) was used as the supporting electrolyte. For methanol oxidation, the experiments were conducted in 10% (2.4 mol L^{-1}) [27], and 57% (13.8 mol L^{-1}) methanol (purchased from Dynamica) in 0.5 mol L^{-1} H$_2$SO$_4$ (purchased from Qhemis). For conversion from measured potential vs. Ag/AgCl electrode (E$_{Ag/AgCl}$) to reversible

hydrogen electrode (RHE) potential (E$_{RHE}$) was employed the Nernst equation:

$$E_{RHE} = E_{Ag/AgCl} + E_{Ag/AgCl}^{\circ} + (0,059 \times pH) \qquad (1)$$

2.5. In situ FTIR

All FTIR spectra were recorded using a Shimadzu IRPrestige-21 spectrophotometer equipped with an MCT detector. The *in situ* FTIR experiments were carried out in a three-electrode spectroelectrochemical cell. A platinum foil and a RHE were used as the counter and reference electrodes, respectively. A modified glassy carbon disc was used as the working electrode (see section 4.2). The cell was equipped with a CaF$_2$ window and was placed on the top of a specular reflectance accessory. *In situ* spectra were collected during chronoamperometry measurements from −0.3 to 1.1 V in a 0.5 mol L^{-1} H$_2$SO$_4$ solution +57% methanol, with and without light at the front side of the electrode. The light source was a UV LED with λ = 365 nm (M365LP1 − Thorlabs). The spectra of possible oxidation patterns of methanol (formic acid, methanol, and formaldehyde) were also recorded using a multiple-reflection ATR accessory (Pike technologies). All spectra were recorded with an average of 256 interferograms with 4 cm^{-1} resolution.

3. Results and discussion

3.1. Characterization of the samples

A valuable tool to characterize the atomically dispersed nickel is the DRIFTS with CO as a probe molecule (Fig. S1, Supporting Information - SI) [28]. CO adsorbs typically on Ni species with two modes: linear adsorption on a single site above 2000 cm^{-1}, or multi coordinate adsorption (bridge), below 2000 cm^{-1} [29]. The peaks in 2040 and 2179 cm^{-1} are related to linearly adsorbed CO, indicative of atomically dispersed nickel sites incorporated in the PHI structure. A fact that strongly corroborates this evidence is the absence of signals in the region of 1900−2000 cm^{-1}, which corresponds to CO bridge and is typical of multiple metals atoms, such as nanoparticles or clusters [25,30−33].

After CO DRIFTS indicates that nickel is incorporated in the form of single atoms in the PHI structure, the amount loaded was quantified using atomic absorption spectroscopy and CHN elemental analysis (Table 1). As expected, in addition to a simple method, the ion exchange treatment proved to be non-destructive and the C/N ratio is almost constant between PHI and Ni−PHI. The quantity of nickel loaded is less than the initial sodium content, which can be explained by the fact that a portion of the sodium present is from sodium chloride remaining from the synthesis and impregnated in the PHI structure. Furthermore, during the cation exchange process, some protons can switch places with sodium, decreasing the C/H ratio shown by Ni−PHI.

In situ infrared Fourier transform spectroscopy with attenuated total reflection spectra of PHI and Ni−PHI (Fig. S2, in SI) exhibit typical absorption bands of the PHI structure, as reported in previous studies [22,34,35]. The vibrations of the heptazine rings can

Table 1
Composition of PHI and Ni−PHI samples (CHN elemental analysis) and metal quantification.

Sample	C (wt. %)	N (wt. %)	H (wt. %)	C/N	C/H	Metal loading (wt. %)
PHI	25.95	40.09	2.11	0.62	12.31	11.3 (Na)
Ni−PHI	22.54	35.70	2.99	0.63	7.54	7.74 (Ni)

be found at 800 cm^{-1} and 1100-1500 cm^{-1}, which presented blue-shifts from PHI to Ni−PHI, being strong evidence for the nickel coordination in the heptazine ring. An increase in surface hydroxyl groups when Ni atoms are coordinated can also be observed, as revealed by the broad band in 2400−3650 cm^{-1}. The presence of water molecules in the coordination sphere of the atomically dispersed metal is very probable. It is clear in Fig. S2 that primary and secondary amines are present in low quantities since no characteristic signal of NH asymmetrical and symmetrical stretching modes can be found at 3000-3500 cm^{-1}. Moreover, less intense bands are observed at 1650 cm^{-1} and 1577 cm^{-1}, which are related to NH bending vibrations [22,36]. This is strong evidence of a low degree of defects and long-range 2D texture of the samples. The coordination of nickel atoms leads to an increase of the vibrations in the region of 1500−1750 cm^{-1} (Fig. S2) and the formation of cyano-groups, assigned to the bands at 2150 cm^{-1} and 2185 cm^{-1}. The presence of metal atoms in the PHI structure shifts the absorption bands of CN stretching to lower wavenumbers, especially in the region of 1050−1275 cm^{-1} (Fig. S2), which evidences the coordination of the metal to the structure and a possible influence on the charge balance of the PHI [25].

For details on the chemical environment of the elements in the TiO$_2$−Ni−PHI film, XPS measurements were performed (Fig. 1). The typical XPS survey spectrum is presented in Fig. 1a and exhibits strong peaks of Ti, C, O, as well as weak peaks of Ni and N. The less evident XPS peaks of Ni and N is because of the low amount of Ni−PHI in the deposition paste (2.5% wt.). The presence of Sn at the XPS survey spectrum is related to the substrate of FTO. The high-resolution Ti 2p spectrum is shown in Fig. 1b and exhibits two well-defined peaks at 458.7 and 464.5 eV that can be assigned to Ti^{4+} 2$p_{3/2}$ and Ti^{4+} 2$p_{1/2}$, respectively [37]. These peaks confirm that Ti is present only as TiO$_2$ on TiO$_2$−Ni−PHI film. The high-resolution C 1s spectrum is presented in Fig. 1c and reveals three peaks assigned to C−C/C]C (284.8 eV), C−O (285.9 eV), and N]C−N (288.5 eV). The C−O peak can be related to adsorbed CO$_2$ molecules or oxygen-contain intermediaries formed during the heat treatment process [38,39]. On the other hand, the presence of sp^2-hybridized carbon N−C]N indicates that the heptazine rings of the carbon nitride structure are still present [40−42]. The high-resolution C 1s spectrum for as-prepared Ni−PHI powder (Figs. S3b and SI) also exhibits peaks assigned to C−C/C]C, C−O, and N]C−N but with a larger N]C−N peak. The high-resolution N 1s spectrum (Fig. 1d) was deconvoluted into sp^2-hybridized nitrogen C−N]C (398.6 eV), ternary N−(C)$_3$ (399.9 eV), and pyrrolic nitrogen C−N−H (401.4 eV) [37,43]. These three types of chemical bonds are involved in the triazine rings and strongly indicate the permanence of the graphitic carbon nitride structure even after heat treatment. A similar high-resolution N 1s spectrum is seen for the Ni−PHI powder as-prepared (Figs. S3c and SI), reinforcing the assertion of the permanence of graphitic carbon nitride structures in the TiO$_2$−PHI (Ni) film. As shown in Fig. 1e, the high-resolution Ni 2p spectrum shows two main peaks at 855.8 and 873.1 eV assigned to Ni^{2+} 2p$_{3/2}$ and 2p$_{1/2}$, respectively. The binding energies and the form of the Ni 2p spectrum are remarkably similar to those observed for Ni(OH)$_2$ indicating that the Ni^{2+} species may be coordinated to hydroxyl groups, the large satellite peaks reinforce this assertion [44]. On the other hand, the high-resolution Ni 2p spectrum of Ni−PHI powder (Figs. S3d and SI) presents bending energy similar to the Ni^{2+} (II) phthalocyanine (856.1 and 874.2 eV) and indicates that Ni^{2+} sites may be stabilized coordinates in PHI structure [45,46].

The diffuse reflectance UV−vis spectra obtained after the thermal treatment (Fig. 2a) exhibits characteristic transitions for the base samples (TiO$_2$, PHI and, Ni−PHI). Pristine TiO$_2$ presents an absorption starting at 380 nm that resembles a semiconductor

band gap onset. In agreement with the linear extrapolating of the Tauc plot curves (Fig. S4), the unmodified TiO$_2$ film shows an allowed direct band gap of 3.25 eV. For PHI and Ni−PHI, an absorption arises at ~430 nm, which is assigned to n-π* transitions involving lone electron pairs on the edge N atoms from the heptazine rings, corresponding to a band gap of 2.75 for both PHI and Ni−PHI, respectively [25,47]. For the modified samples, the TiO$_2$−PHI and TiO$_2$−Ni−PHI samples showed a small red shift in the band gap transitions (for 3.22 and 3.20 eV, respectively) when compared to unmodified TiO$_2$, implying the formation of tight, chemically bonded interfaces between the TiO$_2$ and PHI structures [48].

In the XRD data (Fig. 2b), the peak at 8.28° observed for PHI and Ni−PHI is due to the (100) reflection of the hexagonal arrangement of the structure derived from the heptazine units [22]. Similarly, the peak around 14.3° corresponds to the (110) diffraction plane, which agrees with the formation of polymerized heptazine structures within the layers [22,49,50]. Both samples show a broad peak between 25 and 28° corresponding to the (002) plane of the graphitic layered PHI; this peak can be deconvoluted into four different peaks for PHI, corresponding to interlayer spaces of d = 3.48 Å, 3.39 Å, 3.32 Å, and 3.23 Å [22]. In contrast to PHI, for Ni−PHI, there is a significant change in the pattern of this peak, with a more intense peak around 28°. This change may be attributed to a lattice spacing between the layers of PHI and their charge balance after the exchange of Na$^+$ cations by Ni^{2+} [25].

XRD data for TiO$_2$−Ni−PHI and TiO$_2$ (Fig. 2c) showed high crystallinity and well-defined peaks, which can be indexed to the anatase tetragonal structure of TiO$_2$ according to the JCPDS card 21−1272. The small amount of Ni−PHI yields a small displacement of ~0.2° that may be related to the incorporation of the carbon nitride into the TiO$_2$ matrix.

As shown in the surface micrographs of the TiO$_2$−Ni−PHI sample (Fig. 3 (a)), the deposit is formed by granular nanoparticles homogeneously distributed over the surface of the FTO, similarly to other reported TiO$_2$-nanoparticle films [51]. Fig. 3 b and c show the sample with 1 and 30 layers deposited, respectively. The thickness of 1-layer was difficult to determine precisely, leading to an approximated value of 95 nm, while for the 30-layer film the thickness was 4.35 μm. As the film thickness increase with the number of layers, there is a clear change in the opacity (Fig. S5), due to this, the light-harvesting and, consequently, the PEC performance is affected, as will be further discussed in section 3.2. From TEM images (Fig. 3 d and e), it is possible to observe how the insertion of Ni−PHI affected the TiO$_2$ crystallinity. While pristine TiO$_2$ (Fig. 3 d) presents well-defined particle edges, the edges of TiO$_2$−Ni−PHI particles (Fig. 3 e) were more amorphous. Further, the ImageJ® software allowed the calculus of interplanar distance (d spacing) of the samples, which increase from 0.367 nm for TiO$_2$, in agreement with literature values for anatase (101) [52,53], to 0.389 nm for TiO$_2$−Ni−PHI, befitting with the incorporation of Ni−PHI as observed in the XRD displacement.

3.2. PEC performance

To assess the activity of the photoanodes concerning the OER, linear sweep voltammetry measurements (Fig. 4a) were carried out. The samples PHI, Ni−PHI, and TiO$_2$ films showed a low activity for OER, with almost negligible photocurrent density even at high overpotentials. The poor activity of TiO$_2$ and carbon nitride is in agreement with reports in the literature for these materials [54,55]. On the other hand, although the TiO$_2$−PHI film had a low photocurrent (8.8 μA cm^{-2} at 1.23 V vs. RHE), the value was much higher than that obtained from the PHI film at the same potential (0.3 μA cm^{-2}), indicating a synergistic interaction between TiO$_2$ and
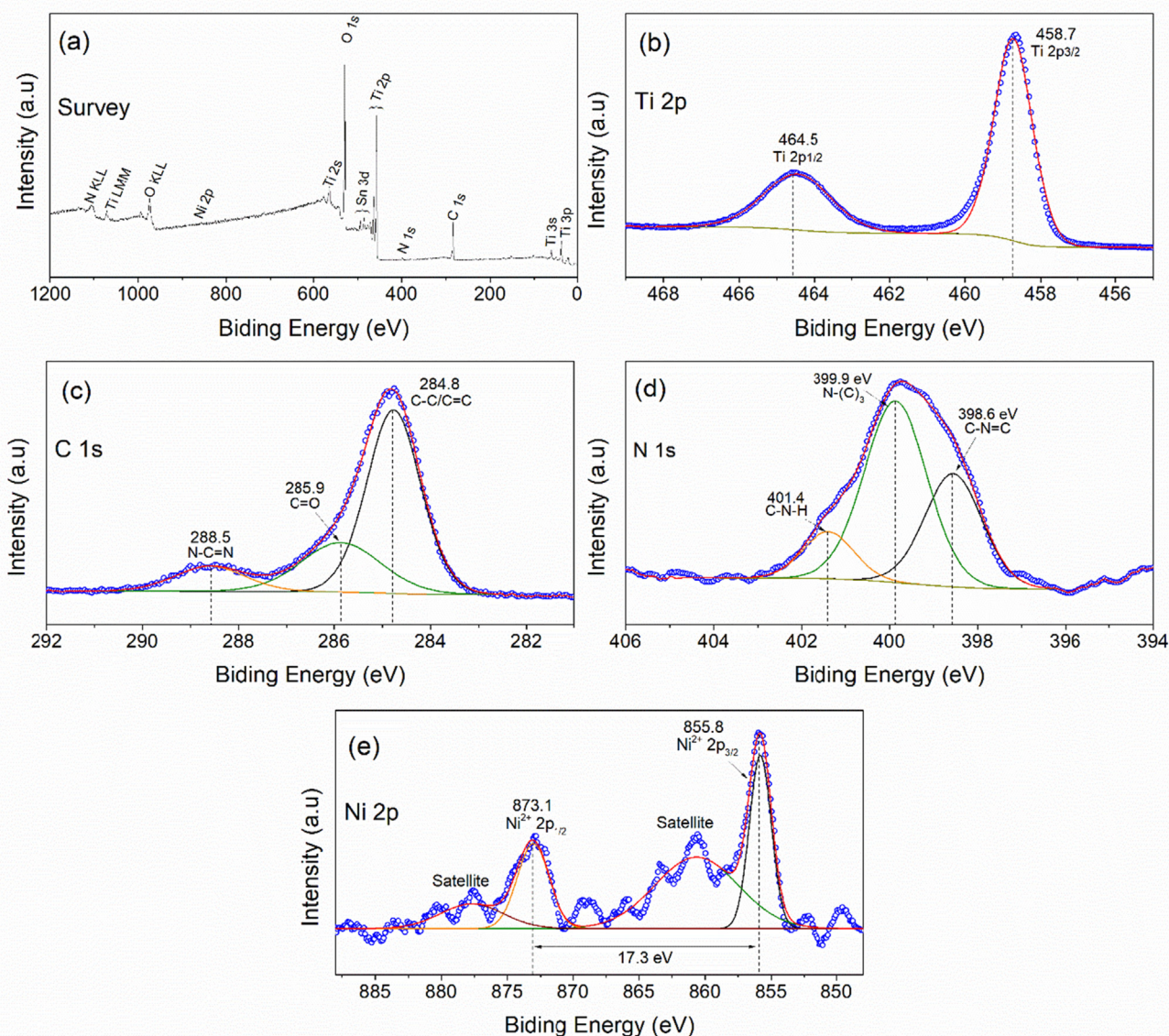
Fig. 1. a) XPS full-spectrum and high-resolution spectra of (**b**) Titanium 2*p*, (**c**) Carbon 1*s*, (**d**) Nitrogen 1*s*, and (**e**) Nickel 2*p* of the TiO$_2$−Ni−PHI film. XPS, X-ray photoelectron spectroscopy.
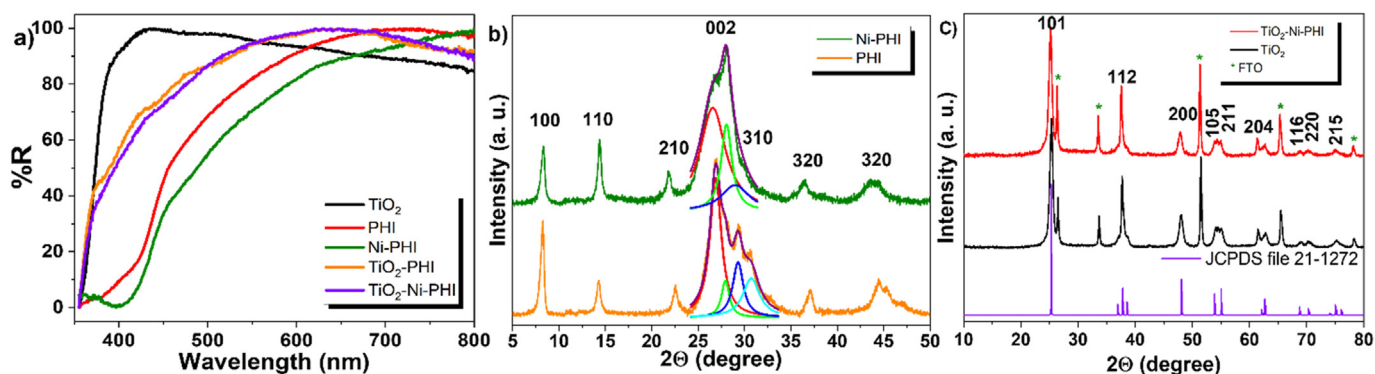

Fig. 2. a) DR UV−vis spectra of PHI, Ni−PHI, TiO$_2$, TiO$_2$−PHI, and TiO$_2$−Ni−PHI. (**b**) XRD spectra for PHI and Ni−PHI, showing the deconvolution of peak (002). (**c**) XRD spectra of TiO$_2$, TiO$_2$−Ni−PHI, and the JCPDS data for anatase TiO$_2$. DR UV−vis, diffuse reflectance UV−vis; PHI, poly (heptazine imide); XRD, X-ray diffraction.
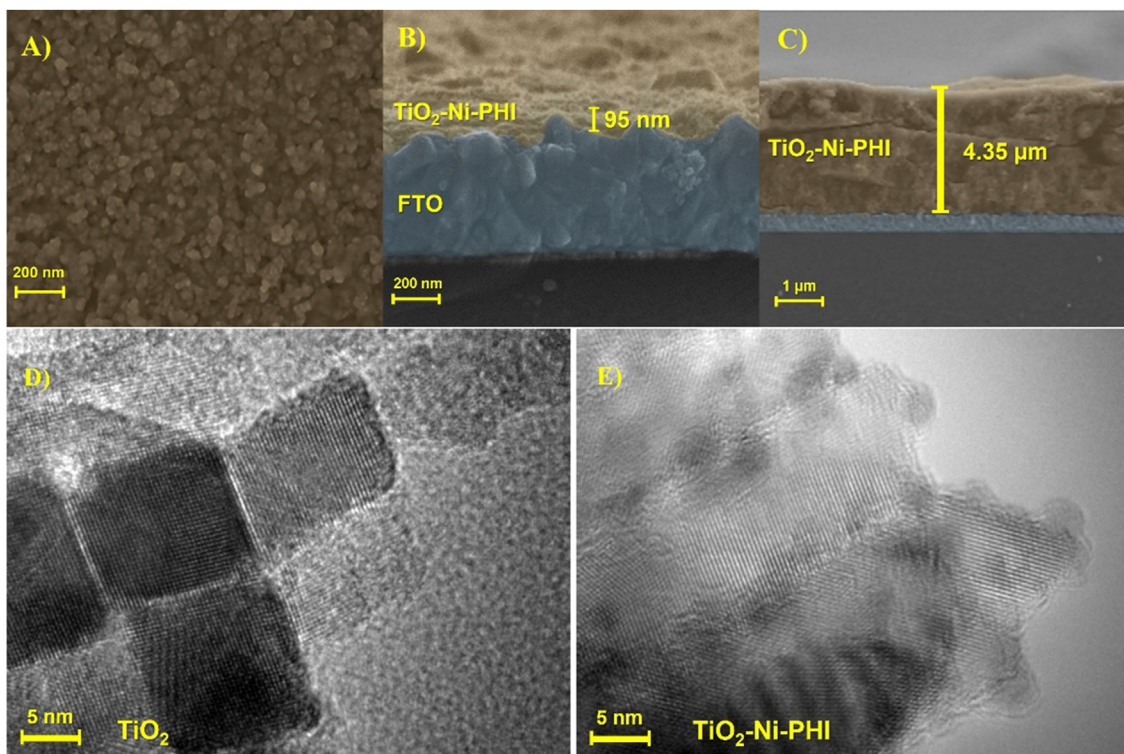
Fig. 3. SEM images of the (**a**) surface of the 1-layer TiO$_2$−Ni−PHI film and cross-sections of the (**b**) 1-layer and (**c**) 30-layer TiO$_2$−Ni−PHI films. The images were colored to highlight the regions containing the film. TEM images of (**d**) TiO$_2$ and (**e**) TiO$_2$−Ni−PHI. PHI, poly (heptazine imide); SEM, scanning electron microscope; TEM, transmission electron microscopy.
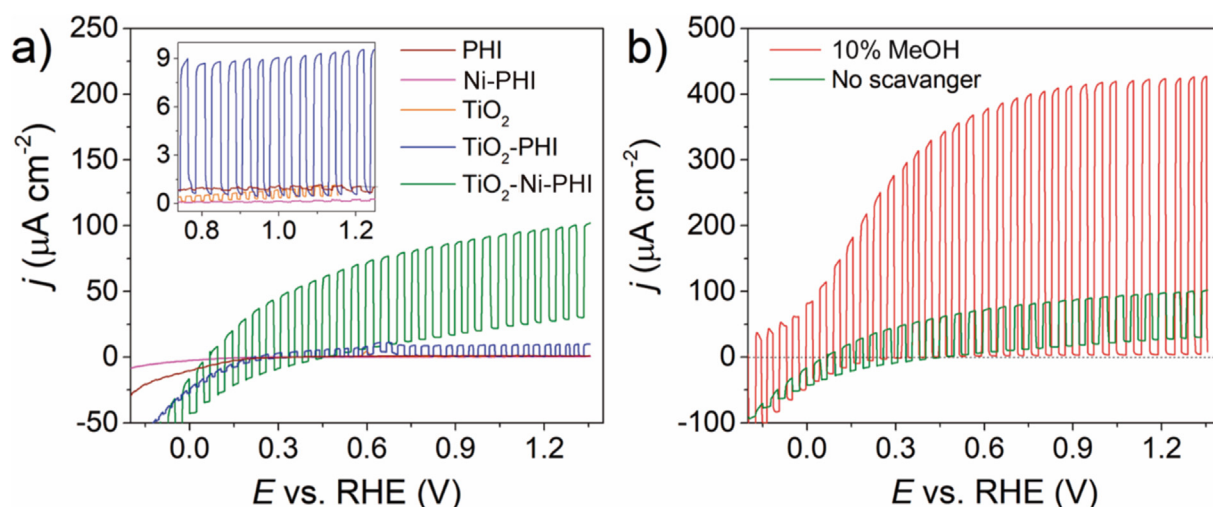

Fig. 4. LSVs curves under chopped light in N$_2$ saturated atmosphere of (**a**) 1-layer films of PHI, Ni−PHI, TiO$_2$, TiO$_2$−PHI, and TiO$_2$−Ni−PHI in Na$_2$SO$_4$ 0.5 mol L^{-1} electrolyte (pH 6), and of (**b**) one-layer TiO$_2$−Ni−PHI films in 10% (V/V) methanol in Na$_2$SO$_4$ 0.5 mol L^{-1} solution, under UV irradiation (365 nm, 90 mW cm^{-2}). LSV, linear sweep voltammetry; PHI, poly (heptazine imide).

the carbon nitride structure. The conduction band and valence band position values were determined with illuminated open cir-cuit potential and Mott-Schottky (Fig. S6 in SI), the energies for TiO$_2$ (−0.06 and 3.19 V vs. RHE), PHI (−0.24 and 2.51 V vs. RHE), and Ni−PHI (−0.94 and 1.81 V vs. RHE) indicate the formation of a type II heterojunction favored. The noteworthy difference between the bands of PHI and Ni−PHI is due to the Ni^{2+} ion coordination, which leads to much stronger delocalized lead to strong delocalization of HOMO/LUMO orbitals from heptazinic rings [56]. The formed

heterojunction ensures better charge separation, reducing the recombination of the electron-hole pair, thus, providing a signifi-cant increase in the PEC activity. Another point that can explain the better photoresponse of the modified samples in comparison to pristine TiO$_2$ is the interference in crystallinity, caused by the insertion of nitrides, as seen in the TEM images. Less organized and amorphous portions in the TiO$_2$ structures can contain substantial electronic defects, favor hole conduction, then enhance the pho-toanode performance. Furthermore, the best PEC activity was

achieved for the TiO$_2$−Ni−PHI film, which presented a photocurrent of 70.3 μA cm^{-2} at 1.23 V vs. RHE. Hence, the photocurrent is eight times higher for TiO$_2$−Ni−PHI than TiO$_2$−PHI, which may be attributed to the presence of nickel species (such as NiOOH and Ni(OH)$_2$) that act as cocatalysts for this reaction [57,58].

Interestingly, the TiO$_2$−Ni−PHI film with 1-layer showed photoactivity when it was used in the MOR, as shown in Fig. 4b. The high photocurrent obtained when using methanol (417 μA cm^{-2} at 1.23 V vs. RHE) is due to the fast capture of the photogenerated holes by methanol that dramatically accelerates the charge transfer at the semiconductor/electrolyte interface and, consequently, reduces the recombination of the electron-hole pair [43].

In the present study, we evaluated the photoanodes properties in different experimental conditions for MOR, using different light sources (UV and solar simulated radiations) and different concentrations of methanol (10 and 57% *V/V*). Fig. 5 shows the results obtained using solar simulated radiation. The photocurrent increment (Fig. 5a) followed the same order observed for OER: TiO$_2$ < TiO$_2$−PHI < TiO$_2$−Ni−PHI, being the values 99.4, 138.4, and 178.5 μA cm^{-2} at 0.2 V vs. RHE, respectively, due to the above-mentioned roles of the heterojunction, electronics defects, and nickel cocatalyst in the process. Due to the better results found for the TiO$_2$−Ni−PHI sample, the film thickness as a function of deposited layers was conducted, and for 8 and 15 layers, the current increased almost linearly (1.24 and 2.35 mA cm^{-2} at 0.2 V vs. RHE), but for the 30-layers film, despite the increase observed in the photocurrent at the same potential (3.16 mA cm^{-2}), this value was no longer proportional to the thickness, indicating that evaluating a greater number of layers would not be feasible.

The better MOR PEC activity observed for films with greater numbers of layers can be related to the material's absorptivity. The 1-layer TiO$_2$−Ni−PHI film was almost translucent and, therefore, a large portion of the incident light was transmitted. In contrast, the 30-layer TiO$_2$−Ni−PHI film had a high opacity (Fig. S5), indicating that a larger portion of the incident light was absorbed. This was confirmed by the graphs of transmittance vs. wavelength shown in Fig. S7 (SI), which show the smallest transmittance for the 30-layer film.

Fig. 5b shows the photocurrent transient recorded at 0.2 V vs. RHE under pulsed illumination for the 30-layer TiO$_2$−Ni−PHI film. No current spikes were observed when turning on the lighting; this

was verified in the four light-dark transients. In general, this behavior indicates a low rate of recombination of charge carriers, suggesting that a large part of the photogenerated holes in the TiO$_2$−Ni−PHI film are used in the MOR. Another point to highlight is the excellent stability of this film, with only 5% of photocurrent decay after 100 min of measurement.

As in the solar simulator, the UV represents a very small portion of the incident radiation (less than 5%), and due to the wide TiO$_2$ bandgap, the same conditions (methanol 10% *V/V*) were studied using a UV LED (365 nm) as a light source. The photocurrent observed for the 30-layers film of TiO$_2$Ni−PHI (Fig. S8) increased to 5.5 mA cm^{-2} at 0.2 V, an increment of almost 75% in comparison with the results under the solar simulator.

Aiming for an even better performance from the photoanodes, we perform further photocurrent measurements with UV irradiation, but with increasing methanol concentrations until reaching a stationary photocurrent density. As can be observed in Fig. 6a, the PHI and Ni−PHI films presented negligible photocurrent responses. On the other hand, the TiO$_2$ film achieved a 109 μA cm^{-2} photocurrent at 0.2 V vs. RHE, while TiO$_2$−PHI and TiO$_2$−Ni−PHI reached 185 and 441 μA cm^{-2}, respectively, at the same potential.

In the same way that the studies performed under solar simulator, the influence of the thickness of the film on the activity for MOR was evaluated (Fig. 6b). A linear increase in the photocurrent with the number of TiO$_2$−Ni−PHI layers was observed up to 15 layers. For the 30-layer film, despite the improved activity, the linearity was not guaranteed, showing a photocurrent of 11 mA cm^{-2} (at 0.2 V vs RHE), which is among the largest photocurrents obtained for the MOR using other photoelectrocatalysts reported in the literature (Table 2). A point to highlight is the behavior of TiO$_2$−Ni-PHI in comparison to benchmark electrocatalysts such as carbon-supported platinum, or bimetallic platinum-ruthenium systems, as long the Pt-based catalysts presents a very low activity for alcohol oxidation in 0.2 V vs. RHE [59−61]. The 30-layer TiO$_2$−Ni-PHI film was able to reach the same magnitude of current (mA cm^{-2}) as those electrocatalysts but without using noble metals.

Aiming for a better understanding of the TiO$_2$−Ni−PHI PEC behavior for the MOR, cyclic voltammetry (CV) was measured for the 15-layer sample both under light and in the dark (Fig. 6c). Both CVs showed peaks of oxidation and reduction between −0.2
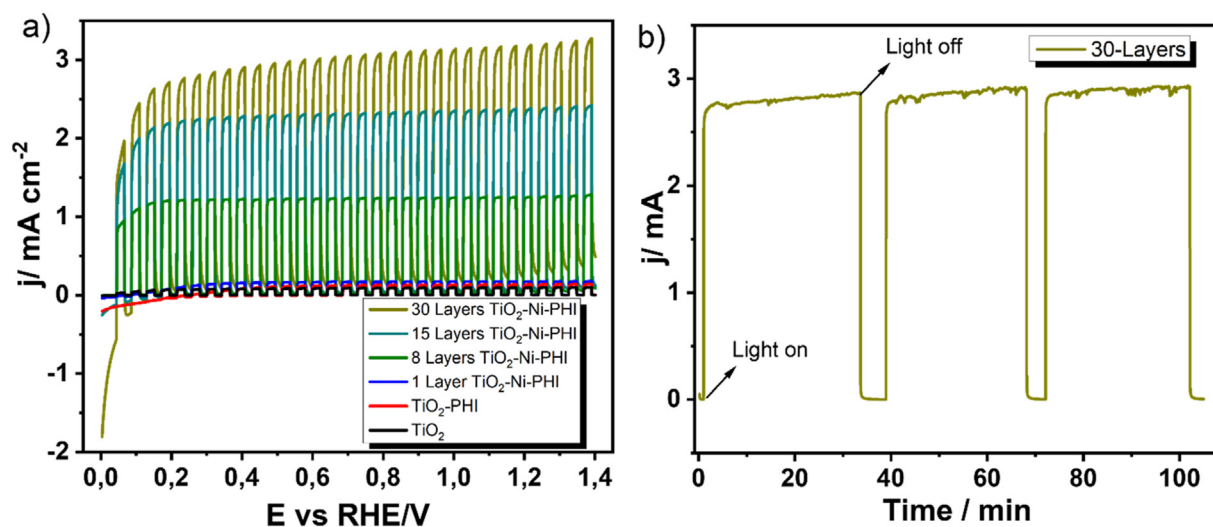

Fig. 5. a) Linear sweep voltammetry (LSV) under chopped light of films of PHI, Ni−PHI, TiO$_2$, TiO$_2$−PHI, and TiO$_2$−Ni−PHI (multiple layers). b) Photocurrent transient for the 30-layer TiO$_2$−Ni−PHI film at 0.2 V vs. RHE. All measurements were performed in N$_2$ atmosphere, 10% (*V/V*) methanol in 0.5 mol L^{-1} H$_2$SO$_4$ electrolyte, under solar simulator (irradiance of 100 mW cm^{-2}). PHI, poly (heptazine imide); RHE, reversible hydrogen electrode.
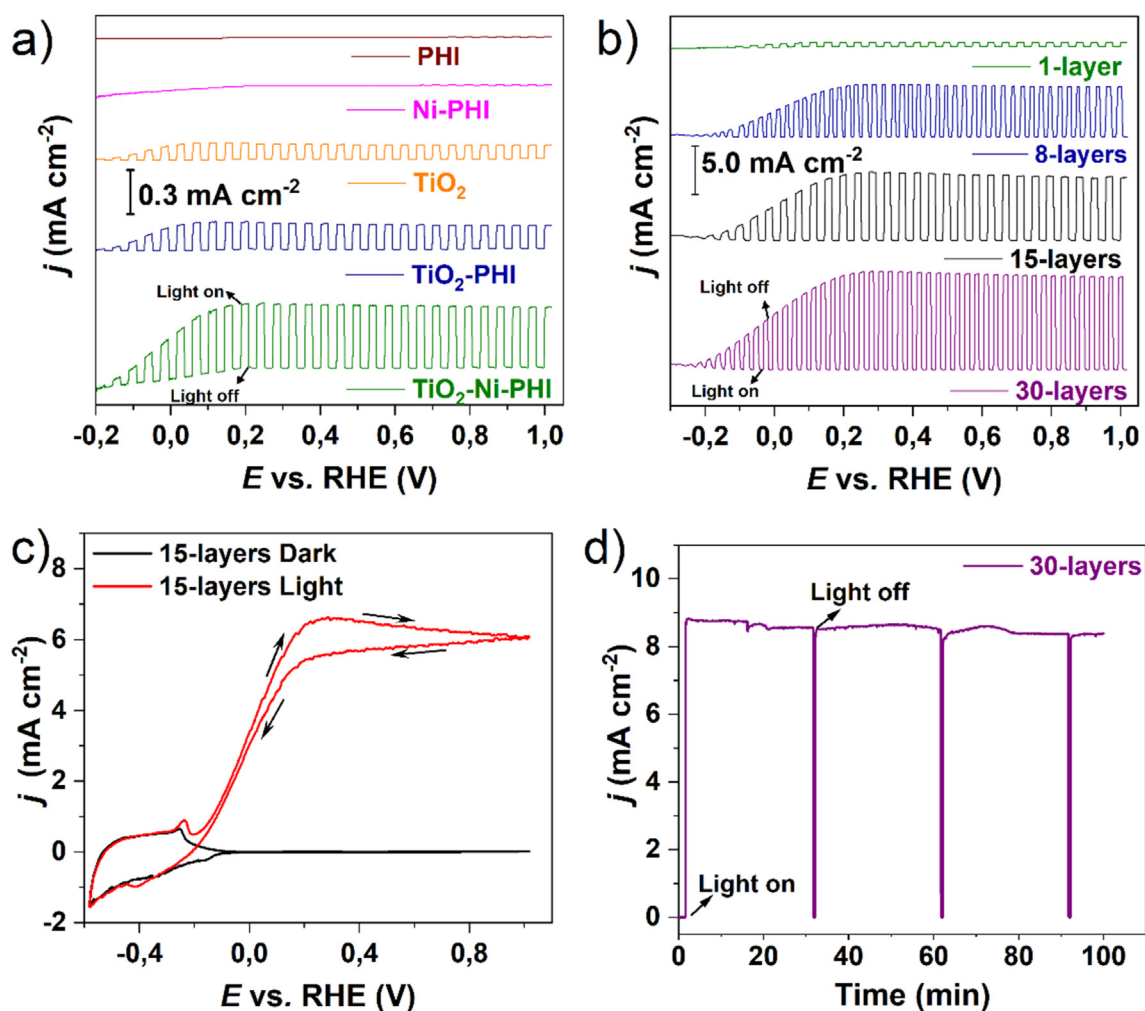
Fig. 6. a) Linear sweep voltammetry (LSV) under chopped light of 1-layer films of PHI, Ni−PHI, TiO$_2$, TiO$_2$−PHI, and TiO$_2$−Ni−PHI. (**b**) LSVs under chopped light of TiO$_2$−Ni−PHI films with different numbers of layers. (**c**) Cyclic voltammetry (CV) for the 15-layer TiO$_2$−Ni−PHI film under illumination and dark and (**d**) photocurrent transient for the 30-layer TiO$_2$−Ni−PHI film at 0.2 V vs. RHE. All measurements were performed in 57% (V/V) methanol in 0.5 mol L^{-1} H$_2$SO$_4$ electrolyte under 365 nm LED illumination (irradiance of 90 mW cm^{-2}). PHI, poly (heptazine imide); RHE, reversible hydrogen electrode.

Table 2
MOR photo-electrocatalysts were recently reported in the literature.

Material	j (mA cm^{-2})	Conditions	Light source	Reference
α-Fe$_2$O$_3$	1.3 (1.0 V vs. RHE)	95% CH$_3$OH in 0.1 mol L^{-1} NaOH	365 nm LED 100 mW cm^{-2}	[8]
CQDs-Pt@Bi$_2$WO$_6$	0.07 (1.07 V vs. RHE)	0.5 mol L^{-1} CH$_3$OH + 1 mol L^{-1} KOH	Solar simulator	[65]
Pt−Ni/TiO$_2$NTs	13.2 (1.19 V vs. RHE)	0.5 mol L^{-1} CH$_3$OH + 1 mol L^{-1} NaOH	500 W Xe lamp	[66]
Pd NPs/TiO$_2$	1.96 (0.88 V vs. RHE)	0.1 mol L^{-1} CH$_3$OH + 0.1 mol L^{-1} HClO$_4$	UV light 150 mW cm^{-2}	[67]
ZnO/α-Fe$_2$O$_3$/Au	0.51 (1.46 V vs. RHE)	95% CH$_3$OH in 0.1 mol L^{-1} NaOH	Xe lamp	[68]
Pt$_{10}$−Au$_1$/CN	1.28 (0.82 V vs. RHE)	1 mol L^{-1} CH$_3$OH + 1 mol L^{-1} KOH	Visible Light	[69]
TiO$_2$−Ni−PHI	**11.0 (0.20 V vs. RHE)**	**57% V/V CH$_3$OH in 0.5 mol L^{-1} H$_2$SO$_4$**	**365 nm LED 90 mW cm^{-2}**	**This work**

CQDs = Carbon Quantum Dots; NTs = Nanotubes; NPs = Nanoparticles; CN = Carbon nitrides.

and −0.4 V. Such processes are associated with the oxidation/reduction of the Ni(OH)$_2$/NiOOH redox couple [62]. In the CV obtained under illumination, no photocurrent hysteresis was observed, indicating that there was no deactivation of the photoelectrocatalyst, e.g. the chemical adsorption of MOR intermediates, such as CO, which is common in Pt-based materials [57,63,64]. The absence of hysteresis in the CV indicates a pathway free of CO poisoning to the MOR mechanism. These features will be discussed ahead based on FTIR *in situ* measurements (Section 3.3). Furthermore, there is almost no Faradaic current in the CV obtained in the

dark, indicating that the MOR occurs mostly under light for TiO$_2$−Ni−PHI. Lastly, the photocurrent transient was recorded at 0.2 V vs. RHE under pulsed illumination for the 30-layer TiO$_2$−Ni−PHI film (Fig. 6d) and followed the same behavior observed in Fig. 5 b). No current spikes when turning on the light (low rate of charge recombination) and small decay after 100 min of measurement (about 5%).

We reinforce that TiO$_2$−Ni−PHI sample showed the best photocurrent density among the studied materials. The 30-layers sample presented photocurrent values among the highest found

recently in the literature for MOR, shown in Table 2. These high photocurrent value in low overpotential (0.2 V vs. RHE) is very important fact when thinking about the practical application of the photoanode. In short, low overpotentials mean lower costs for the construction of efficient devices.

Several effects can explain this observation: the TiO_2 acts as a light absorber, then, the photogenerated holes migrate continually in the PHI structure, oxidizing $Ni(OH)_2$ in the PEC MOR, resulting in NiOOH. Other authors successfully used this species as a catalyst for the electrochemical oxidation of methanol [70,71]. Since NiOOH is an unstable species, it readily oxidizes methanol and later methanol intermediates, regenerating $Ni(OH)_2$. In this context, the high activity of $TiO_2-Ni-PHI$, compared to TiO_2-PHI and unmodified TiO_2 films, was caused by a combination of the TiO_2/PHI heterojunction, that leads to greater charge separation, and the catalysis of the MOR by the NiOOH species, which facilitates charge transfer.

3.3. FTIR in situ measurements

To understand the effect of the light in terms of the intermediates and/or products formed during the MOR, *in situ* FTIR measurements were performed in darkness and under illumination. Fig. 7a shows the results obtained in the dark for $TiO_2-Ni-PHI$ using D_2O as the solvent, where features appeared from -0.2 V vs. RHE in agreement with the electrochemical results. The band at 1200 cm^{-1} is assigned to the presence of SO_4^{-2}, which arises during all potential scans due to the increase in the positive charge of the working electrode, forcing the migration of anions toward the electrode surface. The band centered at 1460 cm^{-1} is assigned to the formation of formaldehyde (for details about the assignment of bands, see Fig. S9 in SI), which means that methanol is being

partially oxidized, even in the absence of light, once the CO_2 is not observed. For the results obtained under UV light with $TiO_2-Ni-PHI$ keeping D_2O as solvent (Fig. 7b), it is also possible to observe the bands corresponding to SO_4^{-2} and formaldehyde. However, the light induces the development of a band at 1710 cm^{-1} and 0.1 V vs. RHE, corresponding to the formation of formic acid. Besides, at 0.3 V vs. RHE, it is observed a band at 2342 cm^{-1}, which is related to CO_2 [10].

In Fig. 7c, the spectra were obtained for $TiO_2-Ni-PHI$ using H_2O as the solvent. This procedure yields complementary data, once the D_2O negatively affects the sensitivity of the method in the region of 2100—2750 cm^{-1}, not allowing the observation of CO_2 production, while water severely influences the region between 1400 and 1800 cm^{-1}, affecting the tracking of the production of formaldehyde and formic acid [72]. In the presence of UV light and water, the formation of CO_2 is evident beginning at 0.2 V vs. RHE. Concomitantly to the CO_2 formation, a consumption band at 2050 cm^{-1} is observed due to the decrease in the quantity of linearly bonded CO. [10,73]. Considering that the material does not present a strong interaction with CO, as shown by the CO DRIFT analysis, there is no observation of surface poisoning and the linearly adsorbed CO (CO_L) can easily be converted into CO_2. Under UV irradiation, more oxidized products are observed such as formic acid (with the transference of 4 e^-) and CO_2 (complete MOR oxidation, transference of 6e^-), while in the dark, only formaldehyde (with the transference of 2e^-) is observed. These different pathways are intrinsically related to the formation of holes/electrons in the semiconductors, and the observed current densities for the photo-electro-oxidation, corroborated by the presented data.

The *in situ* measurements were also conducted for the TiO_2 and TiO_2-PHI samples (Fig. S8), from which it is possible to observe the
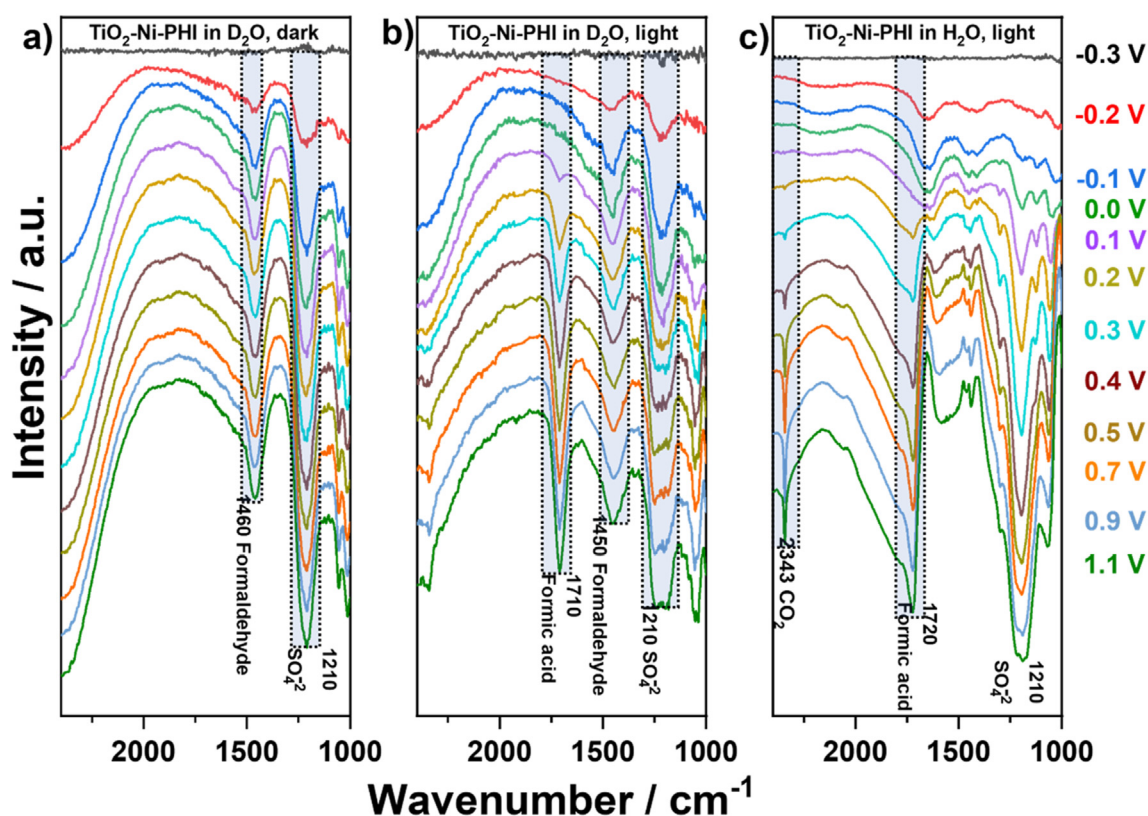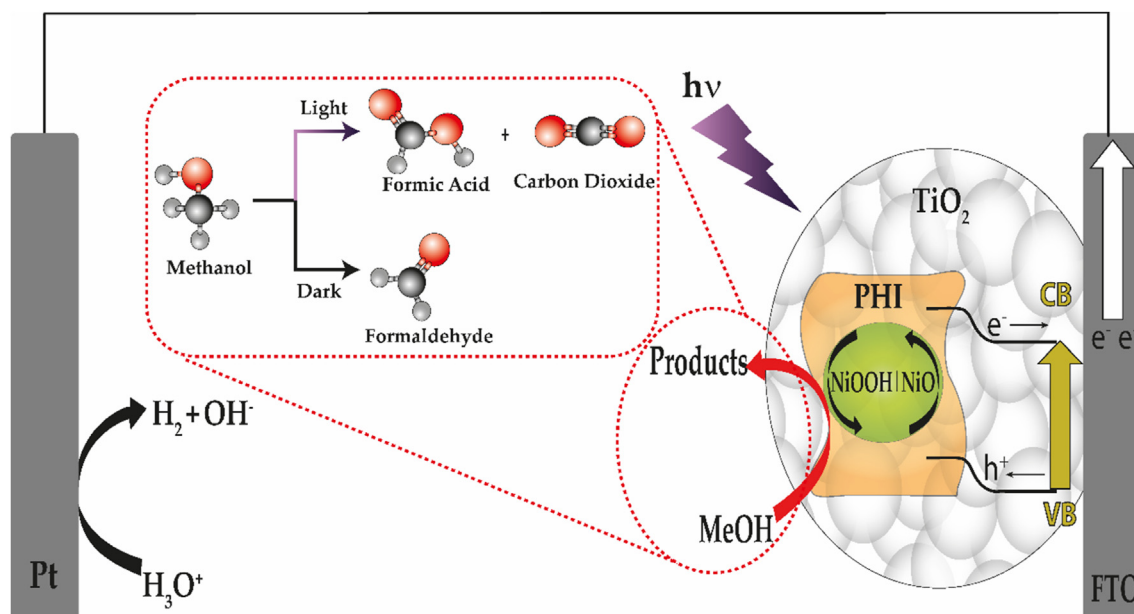

Fig. 7. FTIR spectra obtained at different potentials for TIO$_2$-Ni-PHI in D$_2$O (a) in the dark, (b) under light and (c) in H$_2$O under light, in 0.5 mol L^{-1} H$_2$SO$_4$ solution, 57% V/V methanol. FTIR, infrared Fourier transform; PHI, poly (heptazine imide).

Scheme 2. Schematic illustration of the photoelectrochemical MOR using the $TiO_2-Ni-PHI$ catalyst and reaction pathways proposed by *in situ* FTIR analyses. FTIR, infrared Fourier transform; MOR, methanol oxidation reaction.

same signals as for $TiO_2-Ni-PHI$; this indicates that the MOR follows the same MOR pathway in the three samples. The TiO_2 and TiO_2-PHI samples directly use the photogenerated holes leading to the same products, however, with lower efficiency. For the $TiO_2-Ni-PHI$ sample, the reaction takes place through the oxidation of NiO sites to NiOOH, which acts as a cocatalyst (Scheme 2). Combining the results obtained in water and D_2O, *in situ* FTIR provides information about the reaction mechanism. In the absence of light, the electrode polarization at -0.2 V vs. RHE can convert methanol to formaldehyde only. However, with the incidence of light, molecules of higher oxidation degrees are obtained, and formaldehyde is oxidized through parallel or consecutive pathways to formic acid at 0.1 V vs. RHE and even to CO_2 at 0.2 V vs. RHE or higher potential, as summarized in Scheme 2.

Observing amongst the formed products, formic acid has a high added value for the industry [74]. Although in this work, the quantification and selectivity of the products has not been performed, the application of the obtained photoanode in a photo-electrolyzer is encouraged because aiming to produce concomitantly high purity hydrogen and formic can compensate for the financial cost of inserting methanol in the system. Certainly, the quantification of each of the products and faradaic efficiency data will be considered in future works in the development of photoelectrolyzer devices for the oxidation of organics using the $TiO_2-Ni-PHI$ system."

4. Conclusions

In summary, the modification of TiO_2 with Ni–PHI leads to a photoanode with improved activity for the photo-electro-oxidation of methanol. The characterizations, especially CO DRIFT analysis, indicate the presence of atomically dispersed nickel coordinated on the pyridinic nitrogen groups in PHI. The nickel sites were oxidized during the thermal treatment, leading to NiO, and besides the small quantity of Ni–PHI (2.5 wt %), it influenced the organization of crystal structure of TiO_2 nanoparticles, increasing d spacing, and leading to amorphous portions near the particle edge as observed in TEM images. Also, the Ni–PHI insertion modified the TiO_2 optical

and electronic properties, shifting the band gap of the material, indicating an interaction between the materials that may be one of the factors of improved photoactivity.

The samples that were employed in the MOR displayed the response (photocurrent) in the following order: $TiO_2 < TiO_2-PHI < TiO_2-Ni-PHI$. The progressively better photocurrent can be explained by three factors: (i) amorphous portions near the edges of the particles containing electronic defects; (ii) formation of a heterojunction between TiO_2 and PHI, leading to better charge separation and (iii) the influence of the $Ni(OH)_2$ sites being converted to NiOOH and acting as cocatalysts in the process. A remarkable photocurrent of 11 mA cm^{-2} was reached for the experiments with 30 deposited layers of $TiO_2-Ni-PHI$ under UV radiation and a high concentration of methanol (57% *V/V*), which is comparable to platinum-based materials. Besides the excellent photocurrent obtained, the material also showed good stability, with the photoresponse decreasing about 5% after 100 min in a chronoamperometry.

Finally, *in situ* FTIR provided information about the reaction mechanism and showed that the MOR follows the same reaction pathway for TiO_2, TiO_2-PHI, and $TiO_2-Ni-PHI$; i.e. methanol is oxidized to formaldehyde in the dark and formic acid and CO_2 under light irradiation. This showed that although the materials follow the same pathway, the material modification led to different performances. All those results indicate that the photoanode obtained in the present study has proved itself as a cheap and quite efficient alternative to replacing platinum-based electrodes in future power generation devices, as well can be employed for the concomitant synthesis of products of industrial interest.

Credit authorship contribution statement

Sirlon F. Blaskievicz: Investigation, Methodology, Data curation, Writing — original draft, Writing — review & editing. Hugo L. S. Santos: Investigation, Methodology, Data curation, Writing — original draft, Writing — review & editing. José L. Bott-Neto: Investigation, Methodology, Data curation, Writing — original draft, Writing — review & editing, Ivo F. Teixeira: Visualization,

Writing − review & editing. Pablo Sebastián Fernández: Visualization, Writing − review & editing Lucia H. Mascaro: Visualization, Supervision, Writing − review & editing, Resources.

Declaration of competing interest

The authors declare that they have no known competing financial interests or personal relationships that could have appeared to influence the work reported in this paper.

Acknowledgments

Appendix A. Supplementary data

Supplementary data to this article can be found online at https://doi.org/10.1016/j.mtnano.2022.100192.

References

[1] T.S. Uyar, D. Beşikci, Integration of hydrogen energy systems into renewable energy systems for better design of 100% renewable energy communities, Int. J. Hydrogen Energy 42 (2017) 2453−2456, https://doi.org/10.1016/j.ijhydene.2016.09.086.

[2] A.K. Singh, S. Singh, A. Kumar, Hydrogen energy future with formic acid: a renewable chemical hydrogen storage system, Catal. Sci. Technol. 6 (2016) 12−40, https://doi.org/10.1039/C5CY01276G.

[3] P. Gangadharan, K.C. Kanchi, H.H. Lou, Evaluation of the economic and environmental impact of combining dry reforming with steam reforming of methane, Chem. Eng. Res. Des. 90 (2012) 1956−1968, https://doi.org/10.1016/j.cherd.2012.04.008.

[4] M. Gong, H. Dai, A mini review of NiFe-based materials as highly active oxygen evolution reaction electrocatalysts, Nano Res. 8 (2015) 23−39, https://doi.org/10.1007/s12274-014-0591-z.

[5] R. Van de Krol, M. Grätzel, Photoelectrochemical Hydrogen Production, Springer, New York, 2012.

[6] R. Li, F. Zhang, D. Wang, J. Yang, M. Li, J. Zhu, X. Zhou, H. Han, C. Li, Spatial separation of photogenerated electrons and holes among {010} and {110} crystal facets of BiVO 4, Nat. Commun. 4 (2013) 1−7, https://doi.org/10.1038/ncomms2401.

[7] Y.K. Kho, A. Iwase, W.Y. Teoh, L. Madler, A. Kudo, R. Amal, Photocatalytic H2 evolution over TiO2 nanoparticles. The synergistic effect of anatase and rutile, J. Phys. Chem. C 114 (2010) 2821−2829, https://doi.org/10.1021/jp910810r.

[8] C.A. Mesa, A. Kafizas, L. Francas, S.R. Pendlebury, E. Pastor, Y. Ma, F. Le Formal, M.T. Mayer, M. Gratzel, J.R. Durrant, Kinetics of photoelectrochemical oxidation of methanol on hematite photoanodes, J. Am. Chem. Soc. 139 (2017) 11537−11543, https://doi.org/10.1021/jacs.7b05184.

[9] M. Feng, S. You, N. Cheng, J. Du, High quality perovskite film solar cell using methanol as additive with 19.5% power conversion efficiency, Electrochim. Acta 219 (2019) 356−363, https://doi.org/10.1016/j.electacta.2018.09.195.

[10] T. Iwasita, Electrocatalysis of methanol oxidation, Electrochim. Acta 47 (2002) 3663−3674, https://doi.org/10.1016/S0013-4686(02)00336-5.

[11] W. Li, X. Zhang, X. Zhang, J. Yao, C. Zhan, High-performance solution-processed single-junction polymer solar cell achievable by post-treatment of PEDOT: PSS layer with water-containing methanol, ACS Appl. Mater. Interfaces 9 (2017) 1446−1452, https://doi.org/10.1021/acsami.6b12389.

[12] J. Baltrusaitis, Y.S. Hu, E.W. McFarland, A. Hellman, Photoelectrochemical hydrogen production on α-Fe2O3 (0001): insights from theory and experiments, ChemSusChem 7 (2014) 162−171, https://doi.org/10.1002/cssc.201300715.

[13] H. Gharibi, S. Sadeghi, F. Golmohammadi, Electrooxidation of Ethanol on highly active and stable carbon supported PtSnO2 and its application in

[14] E. Antolini, Photo-assisted methanol oxidation on Pt-TiO2 catalysts for direct methanol fuel cells: a short review, Appl. Catal., B 237 (2018) 491−503, https://doi.org/10.1016/j.apcatb.2018.06.029.

[15] H. He, P. Xiao, M. Zhou, F. Liu, S. Yu, L. Qiao, Y. Zhang, PtNi alloy nanoparticles supported on carbon-doped TiO2 nanotube arrays for photo-assisted methanol oxidation, Electrochim. Acta 88 (2013) 782−789, https://doi.org/10.1016/j.electacta.2012.10.136.

[16] I. Bilecka, P.J. Barczuk, J. Augustynski, Photoanodic oxidation of small organic molecules at nanostructured TiO2 anatase and rutile film electrodes, Electrochim. Acta 55 (2010) 979−984, https://doi.org/10.1016/j.electacta.2009.08.058.

[17] M. Carreño-Lizcano, A.F. Gualdrón-Reyes, V. Rodríguez-González, J. Pedraza-Avella, M. Niño-Gómez, Photoelectrocatalytic phenol oxidation employing nitrogen doped TiO2-rGO films as photoanodes, Catal. Today 341 (2020) 96−103, https://doi.org/10.1016/j.cattod.2019.02.006.

[18] L. Ye, Z. Li, L. Zhang, F. Lei, S. Lin, A green one-pot synthesis of Pt/TiO2/Graphene composites and its electro-photo-synergistic catalytic properties for methanol oxidation, J. Colloid Interface Sci. 433 (2014) 156−162, https://doi.org/10.1016/j.jcis.2014.06.012.

[19] C. Dechakiatkrai, J. Chen, C. Lynam, S. Phanichphant, G. Wallace, Photocatalytic oxidation of methanol using titanium dioxide/single-walled carbon nanotube composite, J. Electrochem. Soc. 154 (2007) 407−411, https://doi.org/10.1149/1.2709498.

[20] F.K. Kessler, Y. Zheng, D. Schwarz, C. Merschjann, W. Schnick, X. Wang, M.J. Bojdys, Functional carbon nitride materials—design strategies for electrochemical devices, Nat. Rev. Mater. 2 (2017) 1−17, https://doi.org/10.1038/natrevmats.2017.30.

[21] D. Ayodhya, G. Veerabhadram, Influence of g-C3N4 and g-C3N4 nanosheets supported CuS coupled system with effect of pH on the catalytic activity of 4-NP reduction using NaBH4, FlatChem 14 (2019) 100088−110098, https://doi.org/10.1016/j.flatc.2019.100088.

[22] Z. Chen, A. Savateev, S. Pronkin, V. Papaefthimiou, C. Wolff, M.G. Willinger, E. Willinger, D. Neher, M. Antonietti, D. Dontsova, "The easier the better" preparation of efficient photocatalysts—metastable poly (heptazine imide) salts, Adv. Mater. 29 (2017) 1700555−1700562, https://doi.org/10.1002/adma.201700555.

[23] M.Y. Ye, S. Li, X. Zhao, N.V. Tarakina, C. Teutloff, W.Y. Chow, R. Bittl, A. Thomas, Cobalt-exchanged poly (heptazine imides) as transition metal−nx electrocatalysts for the oxygen evolution reaction, Adv. Mater. 32 (2020) 1903942−1903948, https://doi.org/10.1002/adma.201903942.

[24] I.F. Teixeira, E.C. Barbosa, S.C.E. Tsang, P.H. Camargo, Carbon nitrides and metal nanoparticles: from controlled synthesis to design principles for improved photocatalysis, Chem. Soc. Rev. 47 (2018) 7783−7817, https://doi.org/10.1039/c8cs00479j.

[25] F.M. Colombari, M.A. da Silva, M. Homsi, B.R. Souza, M. Araujo, J.L. Francisco, G.T. Silva, I.F. Silva, A.F. de Moura, I.F. Teixeira, Graphitic carbon nitrides as platforms for single-atom photocatalysis, Faraday Discuss (2020) 1−9, https://doi.org/10.1039/C9FD00112C.

[26] J. Hulva, M. Meier, R. Bliem, Z. Jakub, F. Kraushofer, M. Schmid, U. Diebold, C. Franchini, G.S. Parkinson, Unraveling CO adsorption on model single-atom catalysts, Science 371 (2021) 375−379, https://doi.org/10.1126/science.abe5757.

[27] K. Trzciński, A. Borowska-Centkowska, M. Sawczak, A. Lisowska-Oleksiak, Photoelectrochemical properties of BIMEVOX (ME=Cu, Zn, Mn) electrodes in contact with aqueous electrolyte, Solid State Ionics 271 (2015) 63−68, https://doi.org/10.1016/j.ssi.2014.10.008.

[28] C. Lentz, S.P. Jand, J. Melke, C. Roth, P. Kaghazchi, DRIFTS study of CO adsorption on Pt nanoparticles supported by DFT calculations, J. Mol. Catal. Chem. 426 (2017) 1−9, https://doi.org/10.1016/j.molcata.2016.10.002.

[29] K.A. Layman, M.E. Bussell, Infrared spectroscopic investigation of CO adsorption on silica-supported nickel phosphide catalysts, J. Phys. Chem. B 108 (2004) 10930−10941, https://doi.org/10.1021/jp037101e.

[30] W. Humphrey, A. Dalke, K. Schulten, VMD: visual molecular dynamics, J. Mol. Graph. 14 (1996) 33−38, https://doi.org/10.1016/0263-7855(96)00018-5.

[31] A.R. Allouche, Gabedit—a graphical user interface for computational chemistry softwares, J. Comput. Chem. 32 (2011) 174−182, https://doi.org/10.1002/jcc.21600.

[32] M. Sun, L. Xu, A. Qu, P. Zhao, T. Hao, W. Ma, C. Hao, X. Wen, F.M. Colombari, A.F. de Moura, Site-selective photoinduced cleavage and profiling of DNA by chiral semiconductor nanoparticles, Nat. Chem. 10 (2018) 821−830, https://doi.org/10.1038/s41557-018-0083-y.

[33] S. Grimme, C. Bannwarth, P. Shushkov, A robust and accurate tight-binding quantum chemical method for structures, vibrational frequencies, and non-covalent interactions of large molecular systems parametrized for all spd-block elements (Z= 1−86), J. Chem. Theor. Comput. 13 (2017) 1989−2009, https://doi.org/10.1021/acs.jctc.7b00118.

[34] A. Savateev, S. Pronkin, M.G. Willinger, M. Antonietti, D. Dontsova, Towards organic zeolites and inclusion catalysts: heptazine imide salts can exchange metal cations in the solid state, Chemistry—An Asian Journal 12 (2017) 1517−1522, https://doi.org/10.1002/asia.201700209.

[35] A. Schwarzer, T. Saplinova, E. Kroke, Tri-s-triazines (s-heptazines)—from a "mystery molecule" to industrially relevant carbon nitride materials, Coord. Chem. Rev. 257 (2013) 2032–2062, https://doi.org/10.1016/j.ccr.2012.12.006.

[36] A. Savateev, S. Pronkin, J.D. Epping, M.G. Willinger, C. Wolff, D. Neher, M. Antonietti, D. Dontsova, Potassium poly (heptazine imides) from amino-tetrazoles: shifting band gaps of carbon nitride-like materials for more efficient solar hydrogen and oxygen evolution, ChemCatChem 9 (2017) 167–174, https://doi.org/10.1002/cctc.201601165.

[37] S. Zhou, Y. Liu, J. Li, Y. Wang, G. Jiang, Z. Zhao, D. Wang, A. Duan, J. Liu, Y. Wei, Facile in situ synthesis of graphitic carbon nitride (g-C3N4)-N-TiO2 heterojunction as an efficient photocatalyst for the selective photoreduction of CO2 to CO, Appl. Catal., B 158 (2014) 20–29, https://doi.org/10.1016/j.apcatb.2014.03.037.

[38] C. Liu, F. Wang, J. Zhang, K. Wang, Y. Qiu, Q. Liang, Z. Chen, Efficient photoelectrochemical water splitting by gC 3 N 4/TiO 2 nanotube array heterostructures, Nano-Micro Lett. 10 (2018) 37–49, https://doi.org/10.1007/s40820-018-0192-6.

[39] B. Zhu, P. Xia, Y. Li, W. Ho, J. Yu, Fabrication and photocatalytic activity enhanced mechanism of direct Z-scheme g-C3N4/Ag2WO4 photocatalyst, Appl. Surf. Sci. 391 (2017) 175–183, https://doi.org/10.1016/j.apsusc.2016.07.104.

[40] B. Zhu, P. Xia, W. Ho, J. Yu, Isoelectric point and adsorption activity of porous g-C3N4, Appl. Surf. Sci. 344 (2015) 188–195, https://doi.org/10.1016/j.apsusc.2015.03.086.

[41] C. Maddi, F. Bourquard, V. Barnier, J. Avila, M.-C. Asensio, T. Tite, C. Donnet, F. Garrelie, Nano-Architecture of nitrogen-doped graphene films synthesized from a solid CN source, Sci. Rep. 8 (2018) 1–13, https://doi.org/10.1038/s41598-018-21639-9.

[42] Y. Lim, J.-I. Heo, M. Madou, H. Shin, Monolithic carbon structures including suspended single nanowires and nanomeshes as a sensor platform, Nanoscale Res. Lett. 8 (2013) 1–9, https://doi.org/10.1186/1556-276X-8-492.

[43] L. Jing, W.-J. Ong, R. Zhang, E. Pickwell-MacPherson, C.Y. Jimmy, Graphitic carbon nitride nanosheet wrapped mesoporous titanium dioxide for enhanced photoelectrocatalytic water splitting, Catal. Today 315 (2018) 103–109, https://doi.org/10.1016/j.cattod.2018.04.007.

[44] A.P. Grosvenor, M.C. Biesinger, R.S.C. Smart, N.S. McIntyre, New interpretations of XPS spectra of nickel metal and oxides, Surf. Sci. 600 (2006) 1771–1779, https://doi.org/10.1016/j.susc.2006.01.041.

[45] P.K. Sonkar, V. Ganesan, R. Gupta, D.K. Yadav, M. Yadav, Nickel phthalocyanine integrated graphene architecture as bifunctional electrocatalyst for CO2 and O2 reductions, J. Electroanal. Chem. 826 (2018) 1–9, https://doi.org/10.1016/j.jelechem.2018.08.020.

[46] H.B. Yang, S.-F. Hung, S. Liu, K. Yuan, S. Miao, L. Zhang, X. Huang, H.-Y. Wang, W. Cai, R. Chen, J. Gao, X. Yang, W. Chen, Y. Huang, H.M. Chen, C.M. Li, T. Zhang, B. Liu, Atomically dispersed Ni(i) as the active site for electrochemical CO2 reduction, Nat. Energy 3 (2018) 140–147, https://doi.org/10.1038/s41560-017-0078-8.

[47] A.B. Jorge, D.J. Martin, M.T. Dhanoa, A.S. Rahman, N. Makwana, J. Tang, A. Sella, F. Cora, S. Firth, J.A. Darr, H2 and O2 evolution from water half-splitting reactions by graphitic carbon nitride materials, J. Phys. Chem. C 117 (2013) 7178–7185, https://doi.org/10.1021/jp4009338.

[48] J. Li, Y. Liu, H. Li, C. Chen, Fabrication of g-C3N4/TiO2 composite photocatalyst with extended absorption wavelength range and enhanced photocatalytic performance, J. Photochem. Photobiol., B 317 (2016) 151–160, https://doi.org/10.1016/j.jphotochem.2015.11.008.

[49] H. Schlomberg, J. Kroger, G.k. Savasci, M.W. Terban, S. Bette, I. Moudrakovski, V. Duppel, F. Podjaski, R.e. Siegel, J.r. Senker, Structural insights into poly (heptazine imides): a light-storing carbon nitride material for dark photocatalysis, Chem. Mater. 31 (2019) 7478–7486, https://doi.org/10.1021/acs.chemmater.9b02199.

[50] J. Fu, J. Yu, C. Jiang, B. Cheng, g-C3N4-Based heterostructured photocatalysts, Adv. Energy Mater. 8 (2018) 1701503–1701533, https://doi.org/10.1002/aenm.201701503.

[51] H.-G. Bang, J.-K. Chung, R.-Y. Jung, S.-Y. Park, Effect of acetic acid in TiO2 paste on the performance of dye-sensitized solar cells, Ceram. Int. 38 (2012) 511–515, https://doi.org/10.1016/j.ceramint.2011.05.065.

[52] D.P. Padiyan, D.H. Raja, Synthesis of various generations titania nanotube Arrays by electrochemical anodization for H2 production, Energy Proc. 22 (2012) 88–100, https://doi.org/10.1016/j.egypro.2012.05.215.

[53] L. Li, Y. Zhang, A.M. Schultz, X. Liu, P.A. Salvador, G.S. Rohrer, Visible light photochemical activity of heterostructured PbTiO3–TiO2 core–shell particles, Catal. Sci. Technol. 2 (2012), https://doi.org/10.1039/C2CY20202F.

[54] L. Ye, D. Wang, S. Chen, Fabrication and enhanced photoelectrochemical performance of MoS2/S-doped g-C3N4 heterojunction film, ACS Appl. Mater. Interfaces 8 (2016) 5280–5289, https://doi.org/10.1021/acsami.5b11326.

[55] J. Safaei, H. Ullah, N.A. Mohamed, M.F.M. Noh, M.F. Soh, A.A. Tahir, N.A. Ludin, M.A. Ibrahim, W.N.R.W. Isahak, M.A.M. Teridi, Enhanced photo-electrochemical performance of Z-scheme g-C3N4/BiVO4 photocatalyst, Appl. Catal., B 234 (2018) 296–310, https://doi.org/10.1016/j.apcatb.2018.04.056.

[56] Q. Chen, H. Dou, S. Zheng, X. Rao, Y. Zhang, Photocatalytic H2 evolution and MB degradation over nickel-doped graphitic carbon nitride microwires under visible light irradiation, J. Photochem. Photobiol., B 382 (2019) 111931, https://doi.org/10.1016/j.jphotochem.2019.111931.

[57] W. Huang, H. Wang, J. Zhou, J. Wang, P.N. Duchesne, D. Muir, P. Zhang, N. Han, F. Zhao, M. Zeng, Highly active and durable methanol oxidation electrocatalyst based on the synergy of platinum–nickel hydroxide–graphene, Nat. Commun. 6 (2015) 1–8, https://doi.org/10.1038/ncomms10035.

[58] F. Lu, M. Zhou, Y. Zhou, X. Zeng, First-row transition metal based catalysts for the oxygen evolution reaction under alkaline conditions: basic principles and recent advances, Small 13 (2017) 1701931–1701948, https://doi.org/10.1002/smll.201701931.

[59] Y. Wang, S. Zou, W.-B. Cai, Recent advances on electro-oxidation of ethanol on Pt-and Pd-based catalysts: from reaction mechanisms to catalytic materials, Catalysts 5 (2015) 1507–1534.

[60] C. He, H. Kunz, J. Fenton, Evaluation of platinum-based catalysts for methanol electro-oxidation in phosphoric acid electrolyte, J. Electrochem. Soc. 144 (1997) 970.

[61] K. Miyazaki, T. Matsumiya, T. Abe, H. Kurata, T. Fukutsuka, K. Kojima, Z. Ogumi, Electrochemical oxidation of ethylene glycol on Pt-based catalysts in alkaline solutions and quantitative analysis of intermediate products, Electrochim. Acta 56 (2011) 7610–7614.

[62] M. Alsabet, M. Grdeń, G. Jerkiewicz, Electrochemical growth of surface oxides on nickel. Part 3: formation of β-NiOOH in relation to the polarization potential, polarization time, and temperature, Electrocatalysis 6 (2015) 60–71.

[63] Y. Ouyang, H. Cao, H. Wu, D. Wu, F. Wang, X. Fan, W. Yuan, M. He, L.Y. Zhang, C.M. Li, Tuning Pt-skinned PtAg nanotubes in nanoscales to efficiently modify electronic structure for boosting performance of methanol electrooxidation, Appl. Catal., B 265 (2020) 118606–118614, https://doi.org/10.1016/j.apcatb.2020.118606.

[64] W. Zhuang, L. He, J. Zhu, R. An, X. Wu, L. Mu, X. Lu, L. Lu, X. Liu, H. Ying, TiO2 nanofibers heterogeneously wrapped with reduced graphene oxide as efficient Pt electrocatalyst supports for methanol oxidation, Int. J. Hydrogen Energy 40 (2015) 3679–3688, https://doi.org/10.1016/j.ijhydene.2015.01.042.

[65] H. Zheng, P. Niu, Z. Zhao, Carbon quantum dot sensitized Pt@ Bi 2 WO 6/FTO electrodes for enhanced photoelectro-catalytic activity of methanol oxidation, RSC Adv. 7 (2017) 26943–26951, https://doi.org/10.1039/C7RA01867C.

[66] H. He, P. Xiao, M. Zhou, Y. Zhang, Y. Jia, S. Yu, Preparation of well-distributed Pt–Ni nanoparticles on/into TiO2NTs by pulse electrodeposition for methanol photoelectro-oxidation, Catal. Commun. 16 (2011) 140–143, https://doi.org/10.1016/j.catcom.2011.09.031.

[67] Y. Xiong, L. Zou, Q. Pan, Y. Zhou, Z. Zou, H. Yang, Photo-electro synergistic catalysis: can Pd be active for methanol electrooxidation in acidic medium? Electrochim. Acta 278 (2018) 210–218, https://doi.org/10.1016/j.electacta.2018.05.052.

[68] B.-F. Zheng, T. Ouyang, Z. Wang, J. Long, Y. Chen, Z.-Q. Liu, Enhanced plasmon-driven photoelectrocatalytic methanol oxidation on Au decorated α-Fe 2 O 3 nanotube arrays, Chem. Commun. 54 (2018) 9583–9586, https://doi.org/10.1039/C8CC04199G.

[69] X. Wang, M. Sun, Y. Guo, J. Hu, M. Zhu, Three dimensional Pt island-on-Au architectures coupled with graphite carbon nitride nanosheets for effective photo-accelerated methanol electro-oxidation, J. Colloid Interface Sci. 558 (2019) 38–46, https://doi.org/10.1016/j.jcis.2019.09.085.

[70] H. He, P. Xiao, M. Zhou, Y. Zhang, Q. Lou, X. Dong, Boosting catalytic activity with ap−n junction: Ni/TiO2 nanotube arrays composite catalyst for methanol oxidation, Int. J. Hydrogen Energy 37 (2012) 4967–4973, https://doi.org/10.1016/j.ijhydene.2011.12.107.

[71] R. Mancharan, J.B. Goodenough, Methanol oxidation in acid on ordered NiTi, J. Mater. Chem. 2 (1992) 875–887, https://doi.org/10.1039/JM9920200875.

[72] P. Christensen, S. Jones, An in situ FTIR study of undoped PolyBenzoImadazole as a function of relative humidity, Polym. Degrad. Stabil. 105 (2014) 211–217, https://doi.org/10.1016/j.polymdegradstab.2014.04.020.

[73] C.D. Silva, P.G. Corradini, L.H. Mascaro, S. Lemos, E.C. Pereira, Using a multiway chemometric tool in the evaluation of methanol electro-oxidation mechanism, J. Electroanal. Chem. 855 (2019) 113598–113604, https://doi.org/10.1016/j.jelechem.2019.113598.

[74] N. Han, P. Ding, L. He, Y. Li, Y. Li, Promises of main group metal−based nanostructured materials for electrochemical CO2 reduction to formate, Adv. Energy Mater. 10 (2020) 1902338.